Crustal structure of China and surrounding regions from *P* wave traveltime tomography

Youshun Sun[1] and M. Nafi Toksöz[1]

Received 26 July 2005; revised 30 November 2005; accepted 19 December 2005; published 21 March 2006.

[1] A three-dimensional (3-D) *P* wave velocity model is developed for the crust and uppermost mantle of China and the surrounding area by applying the tomography method of Zhao et al. using 500,000 high-quality *P* wave first arrivals extracted from the *Annual Bulletin of Chinese Earthquakes* (ABCE). This tomographic method can accommodate velocity discontinuities such as the Moho in addition to smooth velocity variations. The spatial resolution is $1^\circ \times 1^\circ$ in the horizontal direction and 10 km in depth. The velocity images of the upper crust correspond well with the surface geologic features such as basins and the Tibetan Plateau. High-velocity anomalies are found in the lower crust beneath the Precambrian regions (Tarim Basin, Ordos Basin, Sichuan Basin, and western half of Songliao Basin). The highest-velocity anomaly is beneath the Sichuan Basin. High- and low-velocity anomalies imaged beneath the Bohai Gulf are associated with the presence of a major Cenozoic rift system. In the lower crust beneath the South China Block, *P* wave velocities are lower in the north than in the south. The Indochina Block shows low velocities both in the crust and in the uppermost mantle due to volcanism. The *Pn* velocities in the Tibet area are higher than those in other areas largely due to thicker crust. Tomographic model significantly reduces the traveltime residuals. Tests conducted by relocating large explosions and earthquakes validate the 3-D velocity model.

Citation: Sun, Y., and M. N. Toksöz (2006), Crustal structure of China and surrounding regions from *P* wave traveltime tomography, *J. Geophys. Res.*, *111*, B03310, doi:10.1029/2005JB003962.

1. Introduction

[2] China and the surrounding area is a seismically active and geologically complex region (Figures 1 and 2). More than 500 earthquakes with magnitudes (*M*) greater than 6.0 occurred in this region between January 1978 and May 2004 (Figure 1). Historically large and destructive earthquakes took place frequently both in east and west China. Most large earthquakes in this region are located at depths of 10 to 20 km. A detailed investigation of the crustal structure is important for understanding the seismotectonics of the region and for assessing and mitigating seismic hazard.

[3] From a geological point of view, there are four Precambrian platforms (Figure 1) in China and the surrounding area [*Lebedev and Nolet*, 2003]: the North China Block, the South China Block, the Tarim Basin, and the Indochina Block. The North China Block, also known as the Sino-Korean Craton, consists of two major Archean (older than 2.5 Ga) continental nuclei surrounded by Paleoproterozoic (about 1.8 Ga) orogenic belts. One nucleus is approximately within the boundaries of the Ordos Basin (Ordos Plateau), and the other, larger one, is beneath and around the Bohai Gulf. Younger orogenic belts are located along the margins of the block. The South China Block includes two major Precambrian elements: the Yangtze Craton and the Cathaysia Block. The Archean nucleus of the Yangtze Craton is approximately within the boundaries of the Sichuan Basin. The Paleoproterozoic basement is found in the vicinity of the basin and to the southwest; the rest of the basement is probably Grenville age (about 1.0 Ga). The Cathaysia Block is situated along the coast (partly in the South China Fold Belt and partly underwater to the east) and is separated from the Yangtze Craton by orogenic belts of different ages, from about 1000 to 150 Ma. The Tarim Basin consists of a nucleus of Archean through Proterozoic age covered by thick Cenozoic sediments. The Indochina Block also has a Precambrian core and probably extends to the northwest as the Shan Thai (Simao) Block.

[4] The available *P* wave velocity models of the crust and upper mantle in China and the surrounding area have been obtained using a variety of approaches. Global models such as CUB 1.0 [*Shapiro and Ritzwoller*, 2002] and the SAIC $1^\circ \times 1^\circ$ model [*Stevens et al.*, 2001] were constructed from group and phase velocity dispersion measurements of surface waves. The models based on surface waves are generally large-scale and intended to map the deep structure of the earth. The global model CRUST 2.0 (G. Laske et al., CRUST 2.0: A new global crustal model at 2×2 degrees, 2001, available at http://mahi.ucsd.edu/Gabi/rem.dir/crust/crust2.html, last accessed July 2005) was constructed from seismic refraction data and developed from the CRUST 5.1

[1]Earth Resources Laboratory, Department of Earth, Atmospheric, and Planetary Sciences, Massachusetts Institute of Technology, Cambridge, Massachusetts, USA.

0148-0227/06/2005JB003962$09.00

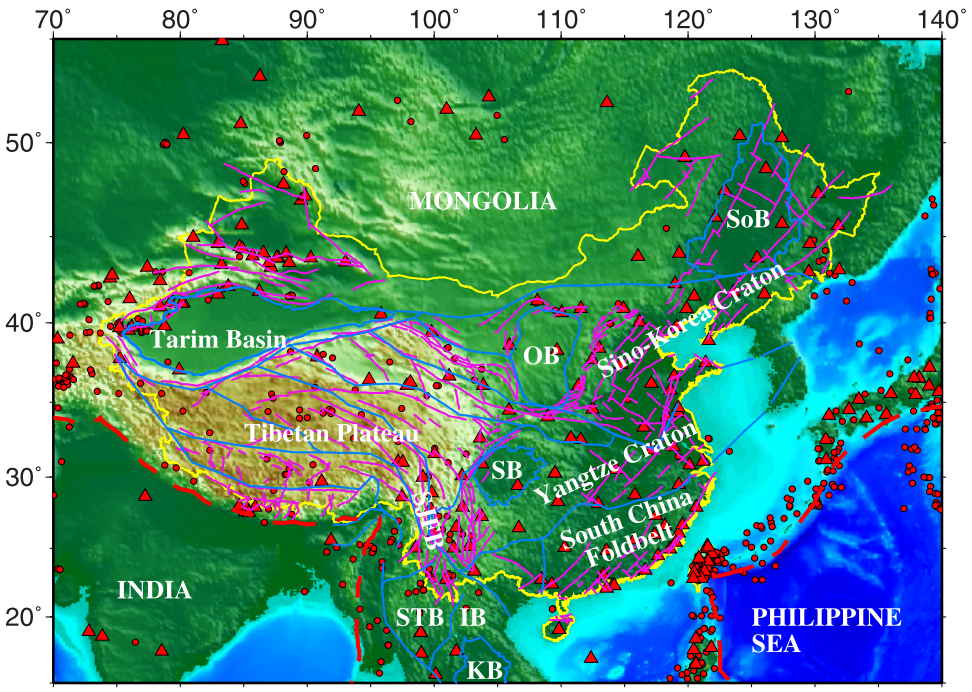

Figure 1. The 512 big earthquakes ($M > 6.0$ from January 1978 to May 2004), 220 stations, active faults and major tectonic boundaries in China and the surrounding area. Earthquake epicenters are shown as red dots, and stations are shown as red triangles. The yellow line shows the boundary of China. Active faults in the China area are shown as purple lines, and tectonic sutures are shown as blue lines, where SoB, Songliao Basin; OB, Ordos Basin; SB, Sichuan Basin; SJFB, Sanjiang Fold Belt; STB, Shan Thai Block; IB, Indochina Block; KB, Khorat Basin.

model [*Mooney*, 1998] and a 1° × 1° sediment map [*Laske and Masters*, 1997]. Although CRUST 2.0 was created by tomographic inversion, there are too few deep seismic soundings (DSSs) to provide enough refraction data for a detailed model. Regional models were constructed by *Pn* and/or *Sn* tomography [*Ritzwoller et al.*, 2002; *Hearn et al.*, 2004; *Liang et al.*, 2004; *Pei et al.*, 2004; *Phillips et al.*, 2005], from surface waves [*Song et al.*, 1991; *Wu et al.*, 1997; *Zhu et al.*, 2002; *Huang et al.*, 2003; *Lebedev and Nolet*, 2003], and from *P* wave traveltime tomography [*Liu et al.*, 1990]. The model of *Liu et al.* [1990] was constructed by regional and teleseismic tomography. The maximum and minimum grid spacings in the model of *Liu et al.* [1990] are 5° × 5° and 2° × 2°, respectively, in the horizontal direction and 300 and 45 km in the vertical direction. This model does not include the fine details for local and regional traveltime calculations and precise earthquake locations.

[5] *P* wave tomography has been performed in several local regions in China [*Zhu et al.*, 1990; *Sun and Liu*, 1995; *Huang et al.*, 2002; *Xu et al.*, 2002; *Wang et al.*, 2003; *Yu et al.*, 2003; *Huang and Zhao*, 2004; *Pei et al.*, 2006]. Xu et al. used *P* wave arrival times of local, regional, and teleseismic events recorded by Chinese and Kyrgyzstan seismic networks to tomographically map the crustal and upper mantle velocity structures beneath western China. The grid spacing is 1.5° × 1.5° in the horizontal direction and about 10 km in the crust and 50 km in the uppermost mantle in the vertical direction. Crustal structures beneath north and east China including Beijing and surrounding regions were obtained by *Zhu et al.* [1990], *Sun and Liu* [1995], *Yu et al.* [2003] and *Huang and Zhao* [2004] as the result of their *P* wave tomographic studies. *Huang et al.* [2002] and *Wang et al.* [2003] inverted the lithospheric structure in southwest China from local/regional arrival time data. *Pei et al.* [2006] and *Li et al.* [2006] imaged the mantle beneath East Asia by performing *P* wave traveltime tomography using regional and teleseismic events. These models show detailed crustal structures only in a few regions. A detailed map for the whole China area remains to be developed.

[6] A high-resolution three-dimensional (3-D) velocity model of China is necessary to provide accurate traveltimes for reliable determination of earthquake locations. Large-scale models obtained by the teleseismic tomography technique generally cannot resolve vertical variations in the shallow structure. Regional models can be combined in order to cover a large area, but such models cannot guarantee smooth and consistent transitions between different regions. During the last several years, there have been many digital seismic stations installed in the China area (Figure 1). The large database of high-quality recorded arrival times provides an unprecedented opportunity to determine a detailed 3-D crustal structure under the region. Therefore we introduce a method that constructs a 3-D *P* velocity model for the whole China area based on observed traveltime data.

[7] The starting model for the tomographic study is a 3-D model created with the adaptive moving window (AMW) method [*Sun et al.*, 2004b] using an extensive catalog of 14 years of earthquake arrival time data. The model assumes a layered crust and a one-layer uppermost mantle at each

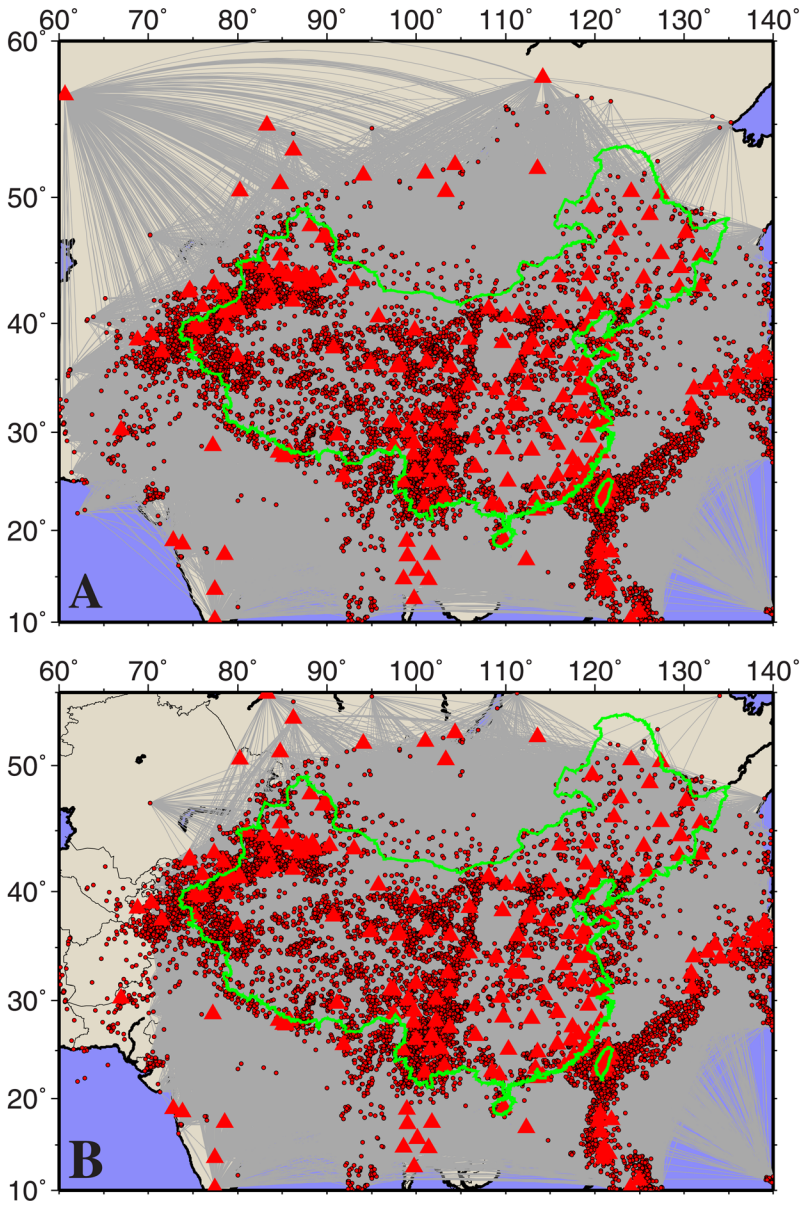

Figure 2. (a) The 25,000 earthquakes, 220 stations, and 500,000 ray paths in China and the surrounding area. Earthquake epicenters are shown as black circles, and stations are shown as red triangles. The green line shows the boundary of China. (b) Distribution of seismic stations and epicenters of selected earthquakes. A total of 16,572 events from *M* 3.0 above are selected.

one degree intersection of longitude and latitude. The thickness and body wave velocity of each layer are found from the observed traveltimes. These 1° × 1° velocity profiles are quilted together with a suitable smoothing to obtain the starting model for the 3-D tomography.

2. Traveltime Data and 3-D Tomography

[8] In this study, we use the earthquake phase data (first *P* wave arrivals) from January 1990 to December 2003 from the ABCE [*Institute of Geophysics, China Seismological Bureau* (*IG-CSB*), 1990–2003]. There are 25,000 earthquakes, 220 stations, and 500,000 ray paths in China and the surrounding area in this database. Figure 2 shows earthquake epicenters, the stations, and the ray paths. We also incorporated special data such as 129 earthquakes with high-quality records and 3 quarry blast events (ground truth events) from Sichuan Province [*Sun et al.*, 2004a].

[9] Given that the ray coverage is denser in some areas and redundant calculation is involved, we adopted the method described below to assemble the best set of the earthquake data. The study area is divided into parallelepipedic blocks with a spatial size of 10 km (northing) × 10 km (easting) × 2 km (depth). Among the earthquakes within each block, we only select the event with the greatest number of first *P* wave arrivals and the smallest hypocentral location uncertainty. As a result, our final data set contains 16,000 events with more than 300,000 ray paths. The final ray coverage has a better (more uniform) distribution in the study area (Figure 2b), and it is

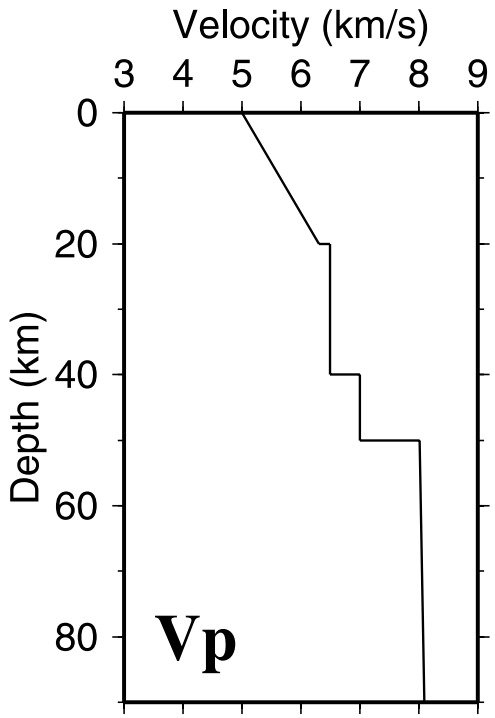

Figure 3. Averaged 1-D velocity model used for the tomographic inversion.

therefore more appropriate for tomographic study than the original data set. Since most aftershocks occur in similar locations with smaller magnitudes and tend to produce larger reading errors for the phase arrivals than the main shocks, the final data set contains the least number of aftershocks.

[10] The input and output 3-D models are represented by velocity perturbations relative to an averaged 1-D reference model in the study area. Even though the traveltimes are calculated based on 3-D models, the 1-D reference model significantly influences the final result of the tomographic study because of the linearization process taken in the tomography. An inappropriate initial reference model may not only affect the quality of the three dimensional images by introducing artifacts, but it may also influence the confidence calculations by underestimating the uncertainties of the results [*Yu et al.*, 2003; *Kissling et al.*, 1994]. We inverted the arrival time data in our selected data set for a 1-D velocity model representing the whole study area by minimizing the root-mean-square (RMS) error of the traveltimes. Finally, we obtained the 1-D model shown in Figure 3 which gave the best fit to the observed data. We used this averaged 1-D model as the reference velocity model for our tomographic inversions.

[11] The discontinuities represent known geological boundaries such as the Conrad and the Moho discontinuities. Previous studies were able to map the Moho discontinuity in the study area and revealed its significant lateral depth variations [*China Seismological Bureau*, 1986; *Li et al.*, 2001; *Sun et al.*, 2004b; Y. Sun et al., The layered crustal structure in China, submitted to *Bulletin of the Seismological Society of America*, 2006]. The Conrad discontinuity is clear only in some regions of the study area, and therefore we only incorporate the Moho discontinuity in this study. The input geometry of the Moho discontinuity was compiled from previous results [*Sun et al.* 2004b]. The Moho is shallower in eastern China, ranging from 30 to 42 km, compared to western China where it is between 50 and 78 km. All the depths are referenced to sea level.

[12] We applied the tomographic method of *Zhao et al.* [1992] for determining the crustal and uppermost mantle velocity structures in China and the surrounding area. Zhao's method, described in detail in several papers [*Zhao et al.*, 1992, 1994; *Zhao*, 2001], allows 3-D velocity variations everywhere in the model and can accommodate velocity discontinuities. The velocity structure is discretized using a 3-D grid. The velocity perturbation at each point is calculated by linearly interpolating the velocity perturbations at the eight surrounding (adjacent) grid nodes. Velocity perturbations at grid nodes are the unknown parameters for the inversion procedure. To calculate traveltimes and ray paths accurately and rapidly, the pseudobending technique [*Um and Thurber*, 1987] and Snell's law are used iteratively. Station elevations are taken into account as station corrections when an averaged 4 km/s crustal velocity model was used. The LSQR algorithm [*Paige and Saunders*, 1982] with a damping regularization is used to solve the large and sparse system of equations. The nonlinear tomographic problem is solved by iteratively conducting linear inversions. At each iteration, perturbations to hypocentral parameters and velocity structure are determined simultaneously. Although we believe that epicentral errors are very small (about 10 km) in the ABCE data set, we have allowed the hypocenters to be relocated in our inversion process in order to solve the inversion problems completely.

3. Implementation and Resolution Analysis

[13] From the checkerboard resolution analyses, we adopt a grid spacing of 1° in the horizontal direction, and 10 km in depth (Figure 4). We add grid nodes at depths of 1 km, 2 km,

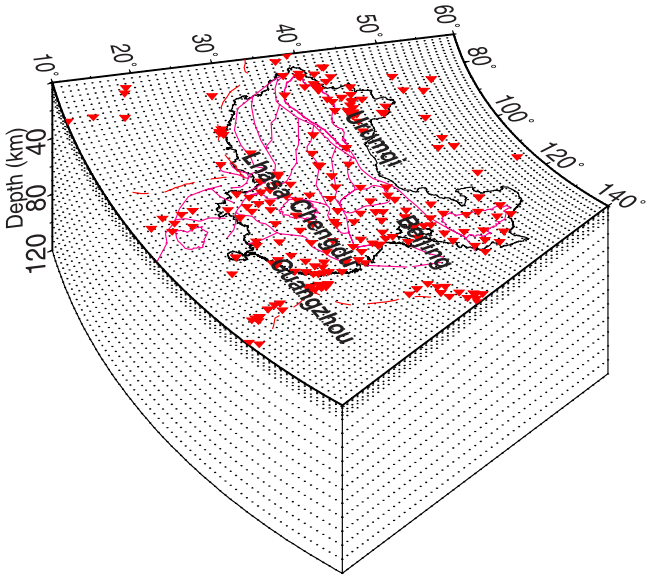

Figure 4. Three-dimensional configuration of the grid adopted in the present study.

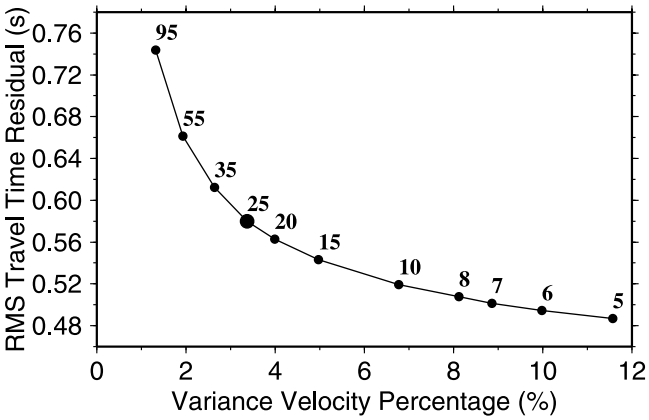

Figure 5. Trade-off curve for the variance of the velocity perturbations and root-mean-square traveltime residuals. Numbers beside the black dots denote the damping parameters adopted for the inversions. The largest black dot denotes the optimal damping parameter for the final tomographic model.

5 km, and 7 km to discretize the sediment layer. We chose a damping value of 25.0 from the tradeoff curve (Figure 5) between the traveltime residuals and the model variance by considering the balance between the reduction of traveltime residuals and the smoothness of the 3-D velocity model obtained [*Eberhart-Phillips*, 1986]. For the inversion with a damping parameter of 25.0, the RMS traveltime residual is reduced from 0.91 s to 0.58 s, and the variance reduction is 57% between the initial and final 3-D models. Figure 6 shows the change in the distribution of traveltime residuals before and after the inversion. Over 80% of the rays have residuals smaller than 0.45 s after the inversion (Figure 6). Figure 6 also shows that the RMS traveltime residual is about 1.2 s if the 1-D reference model is used to calculate the traveltimes. The variance reduction is

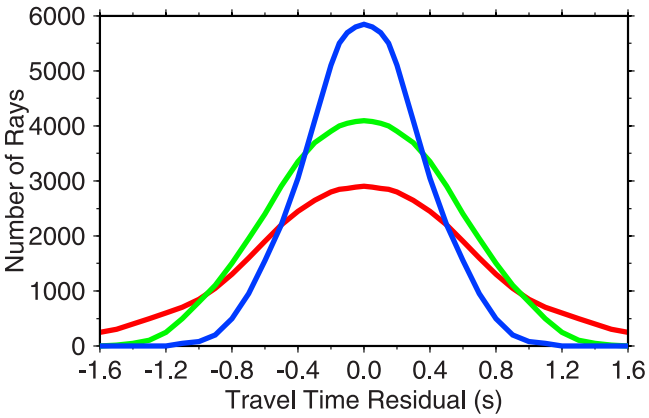

Figure 6. Distributions of traveltime residuals. The red line denotes the result for the averaged 1-D model. The green line denotes the result for the starting model (before the inversion). The blue line denotes the result after the inversion.

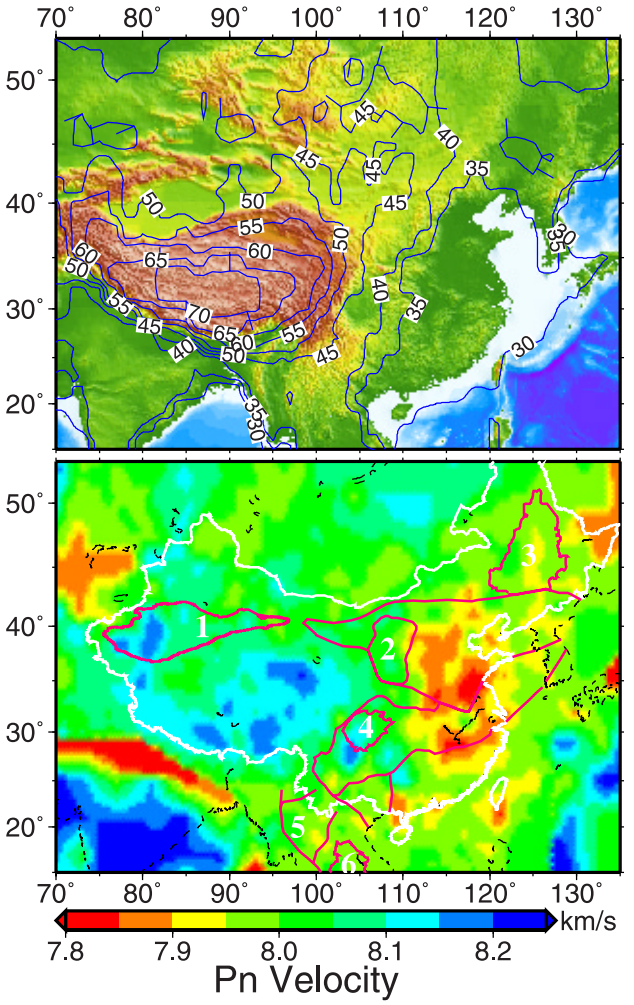

Figure 7. Depth distribution of (top) the Moho discontinuities and (bottom) the *Pn* velocities in the study area. The Moho depths are shown in contours. 1, Tarim Basin; 2, Ordos Basin; 3, Songliao Basin; 4, Sichuan Basin; 5, Shan Thai Block; 6, Khorat Basin.

about 70% between the final 3-D model and the averaged 1-D model.

[14] The distribution of hit counts (number of rays passing through each grid node) for each layer [*Sun*, 2005] shows that most parts of the study area are well sampled by the rays. The Tianshan area, the Sichuan-Yunnan area including eastern Tibet, and southeastern China including Taiwan are the regions with the most ray coverage at all depths. Ray coverage in the crust under north China is also very dense. Intuitively, given such extensive ray coverage, we expect a model with high spatial resolution. We will examine the model resolution in a systematic manner later.

[15] The Moho variations and *Pn* velocities are shown in Figure 7. Figure 8 shows 3-D *P* wave velocity variations at depths of 10, 20, 30, 40, 60, and 80 km. Vertical cross sections of the velocity images along the profiles denoted in Figure 9 are shown in Figures 10 and 11. The tomographic images are shown in areas with hit counts greater than 8.

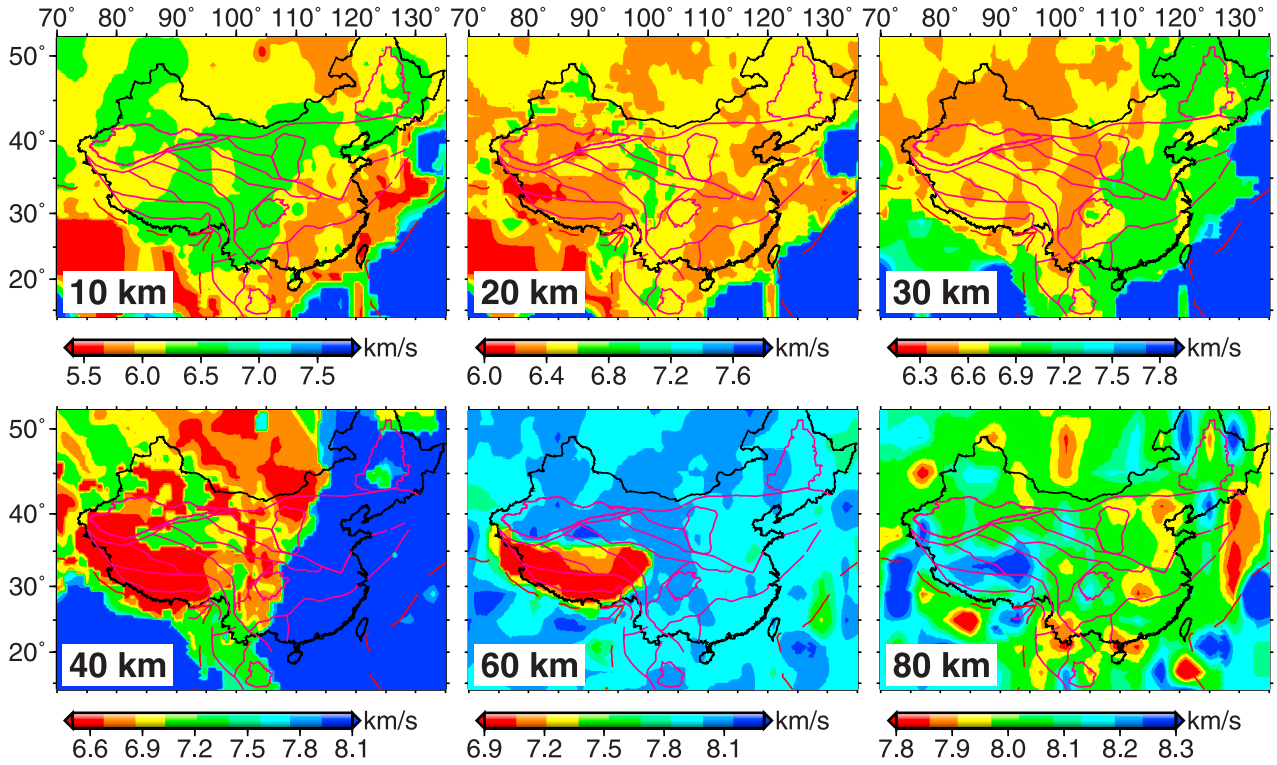

Figure 8. *P* wave velocity image at each depth slice. The depth of each layer is shown at the lower left corner of each map.

[16] Before analyzing the results of the tomographic inversion, we perform tests with synthetic data to evaluate the resolution of the tomographic image. We calculate a set of traveltime delays by tracing the corresponding rays through a synthetic structure such as checkerboard, then we invert the synthetic data for the velocity structure, and finally we compare the inversion result with the initial synthetic model. To make a checkerboard velocity model, we assign ±3% velocity perturbations to the 3-D grid nodes. Random errors from a normal distribution with a standard deviation of 0.1 s are added to the synthetic traveltimes calculated from the synthetic models. *Leveque et al.* [1993] showed that in some cases small structures in a checkerboard test can be retrieved effectively while large structures are poorly imaged. To test for such behavior in our tomographic study, we conduct checkerboard tests with different grid spacings of 1°, 2°, 4°, and 8°.

[17] Figure 12 shows the input checkerboard and the corresponding resolution test results with grid spacings of 1°. The 1° velocity model is best recovered in the Tianshan, the Sichuan-Yunnan and the southeastern China areas to depths smaller than 40 km. This correlates well with hit count distribution patterns [*Sun*, 2005]. For depths greater than 50 km, the resolution is high in most of mainland China. While the resolution is high for most Tibetan regions at large depths, part of western Tibet has relatively low resolution. From these resolution tests, we infer that for mainland China and the surrounding area, the tomographic images obtained have a spatial resolution of 1° in the horizontal direction and 10 km in depth, and large-scale structures are well resolved. For the peripheral areas of Mongolia and India, structure can be resolved at large grid spacing, such as 8°.

4. Results and Validation

4.1. Results

[18] The 3-D *P* wave velocity model is shown at constant depths in Figure 8. At a depth of 40 km, low-velocity (low-V) zones are visible in the western part of China and high-velocity (high-V) zones exist in the eastern part. A

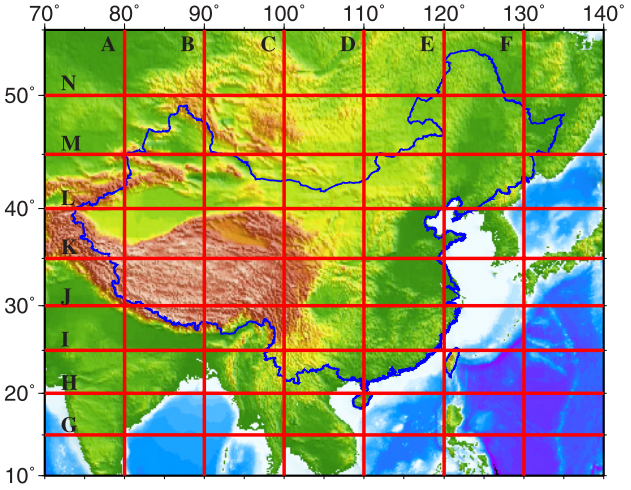

Figure 9. Locations of the vertical cross sections shown in Figures 10 and 11.

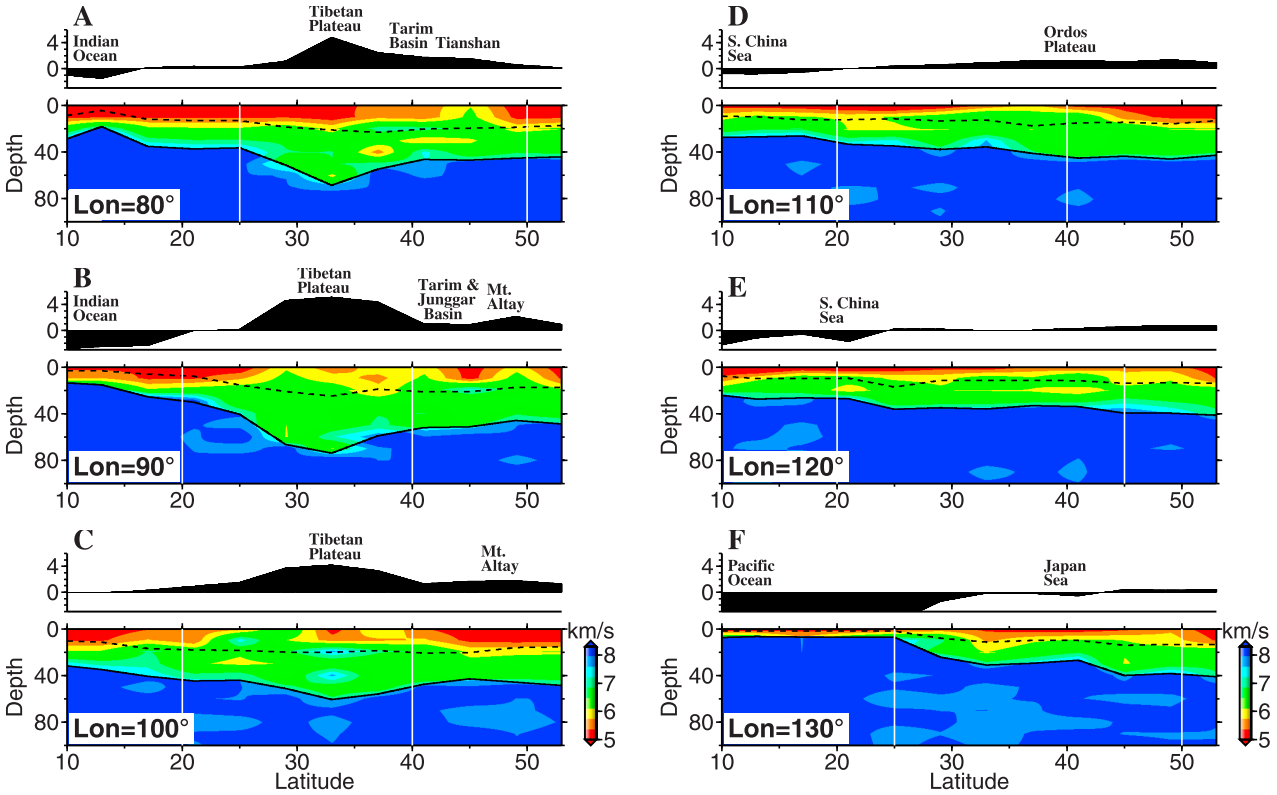

Figure 10. Vertical cross sections of *P* wave velocity when the Moho depth variations (Figure 7) are taken into account. Cross sections A, B, C, D, E, and F at the longitudes of 80°, 90°, 100°, 110°, 120°, and 130° are plotted. The surface topography along each profile is shown on the top of each cross section. The black curved lines show the Conrad (dashed) and Moho (solid) discontinuities. Each grid in the region between the two white lines has a ray path hit count of 200 or above.

clear dividing line appears around 105°E separating the east and west seismic zones in mainland China. At a depth of 60 km, the Tibetan Plateau is clearly outlined as a low-V zone. At a depth of 80 km, the root of the Tibetan Plateau disappears. High-V zones appear in the western and southern part of the Tibetan Plateau. There are a few low-V zones sandwiched between the high-V zones. The deeper velocity slices (60 and 80 km) with scattered low-V zones in eastern China indicate the presence of tectonic extension in the area. These results are consistent with those obtained by a joint inversion of the DSS data from multiple profiles [*Li et al.*, 2001]. Low-V zones beneath the Indochina Block including the Khorat Basin in the crust and uppermost mantle are related to intraplate volcanism [*Lebedev and Nolet*, 2003].

[19] The *Pn* velocity image has a high resolution in the whole study area (Figure 7). *Pn* velocities are low at the center of the Songliao Basin, but high under most of the Tarim Basin, the Sichuan Basin and the Ordos Basin. This result is generally consistent with the recent *Pn* tomography by *Pei et al.* [2004], *Liang et al.* [2004], *Hearn et al.* [2004], and *Phillips et al.* [2005]. Detailed discussion of the *Pn* structure is given in section 5.

[20] Velocity changes are visible across some features such as the Sanjiang Fold Belt. Velocity anomaly is visible from a depth of 10 km to a depth of 30 km, suggesting that some of the faults may have cut through the crust and reached to the middle or lower crust. No velocity contrast is visible across most of the faults, particularly in the middle to lower crust, suggesting that most of the faults may be shallow features in the upper crust. It is also possible that our tomographic model has insufficient spatial resolution to image the fault zones.

4.2. Relocation of GT Events

[21] We test our 3-D model by relocating the GT events (which were excluded from the inversion) and comparing the results with known locations. Eleven GT events are the nuclear explosions in northwestern China from 1990 to 1996, recorded by stations in China and the surrounding area. Only *P* wave arrival times are available in the data set. These events are determined independently using both satellite imagery [*Fisk*, 2002] and seismic data recorded by stations in China and the surrounding area.

[22] The explosions are closely clustered. Table 1 shows the parameters for these nuclear explosions. With our final *P* wave velocity model for the crust and upper mantle in China and the surrounding area, we relocate the GT events using arrival time data recorded at stations within 20° epicentral distance. The relocation errors are also listed in Table 1. The "error" values are the hypocentral difference in kilometers between the reference hypocenters and relocations using the new 3-D *P* wave model, 1-D average China model obtained from the 3-D model, and the AK135 global model.

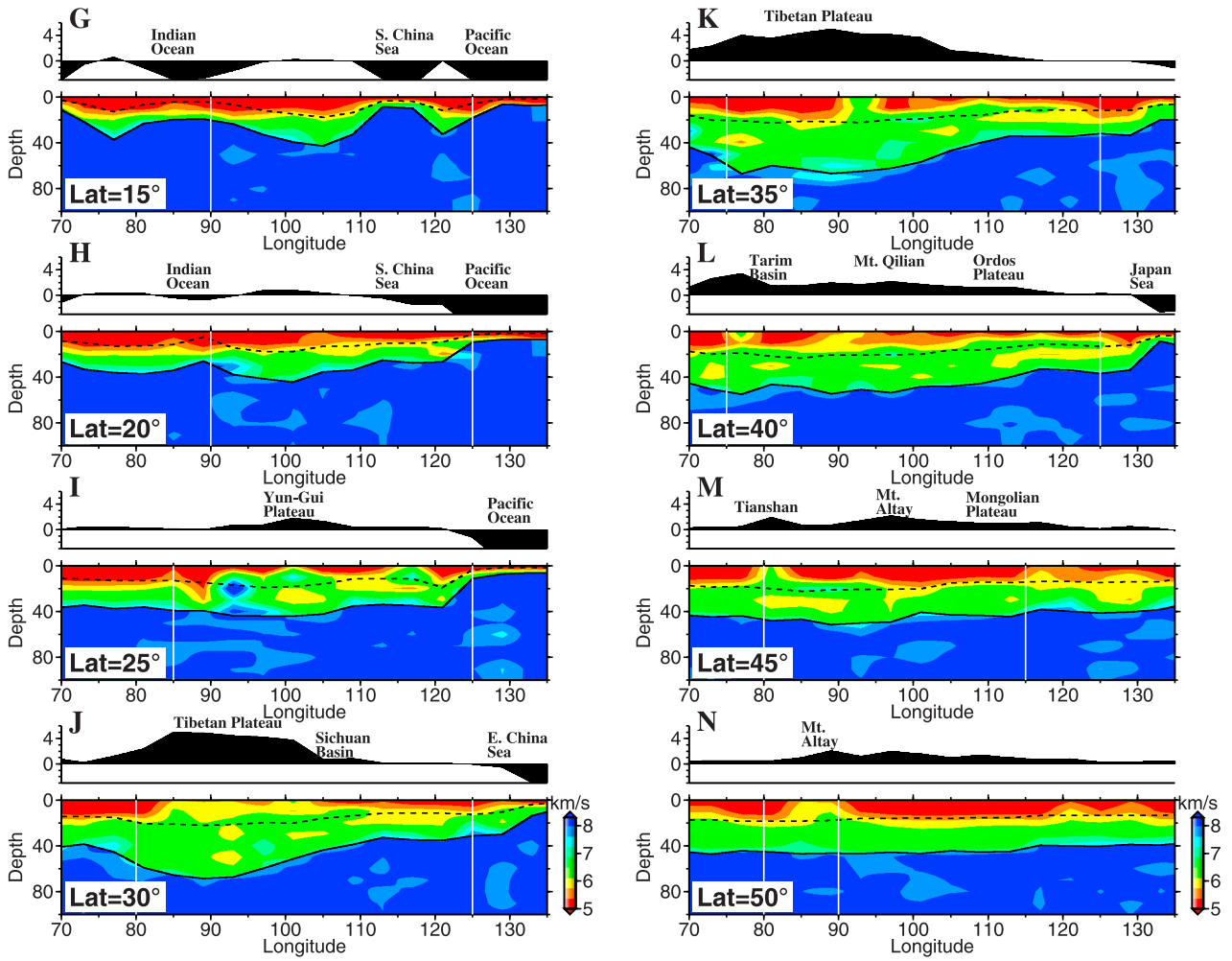

Figure 11. Same as Figure 10 except for cross sections G, H, I, J, K, L, M, and N at latitudes of 15°, 20°, 25°, 30°, 35°, 40°, 45°, and 50°.

[23] The averaged hypocentral error of relocation is only 0.7 km with a standard deviation of 0.2 km for our new 3-D *P* wave model. The mean hypocentral misfit is about 10 km if the averaged 1-D velocity in China is used, and the misfit is about 20 km if the global AK135 model is used. Even though the GT events are located in northwestern China with most stations distributed in southern and eastern China, the small relocation errors clearly suggest that an accurate *P* wave velocity model gives good event locations with limited azimuthal coverage.

4.3. Traveltime Validation

[24] Another way of validating velocity model is to compare the observed traveltimes from the GT events and earthquakes with the predicted traveltimes calculated with the new model. The eleven explosions essentially occurred in two testing areas (41.55°, 88.73°) and (41.72°, 88.38°). The distance between these two areas is less than 40 km, which is relatively small compared to the average source-receiver distance of 12° from all the selected stations. Instead of comparing the traveltime residuals at each station from each individual event, we calculate the averaged traveltime residual at each station from all the GT events (Table 2). We see that both the traveltime residuals and the standard deviations decrease when the models are used in order of AK135, averaged 1-D, the input 3-D, and the final 3-D.

[25] The mean traveltime residual (our final 3-D model) is smaller than 0.6 s when the stations are within 15° epicentral distance from the events. The traveltime residuals increase to about 0.9 s when the stations are about 20° from the events. The larger traveltime residuals observed at greater distances are due to the fact that our final 3-D model is inverted using the arrival times with the source-receiver distance smaller than 15°. The deeper structures (deeper than 200 km) of the model are less constrained by regional arrival time data in our tomographic study. The standard deviations are smaller than 0.2 s. These results clearly confirm that the *P* wave model we obtained from traveltime tomography in the crust and uppermost mantle is accurate.

[26] It is also important to compare the traveltimes from the earthquakes with well constrained hypocenters. Since all explosions (GT events) are located in the northwest part of China, with a 20° limit in epicentral distance from station to event, the model structure in the eastern part of China is not validated by relocating the GT events or comparing the

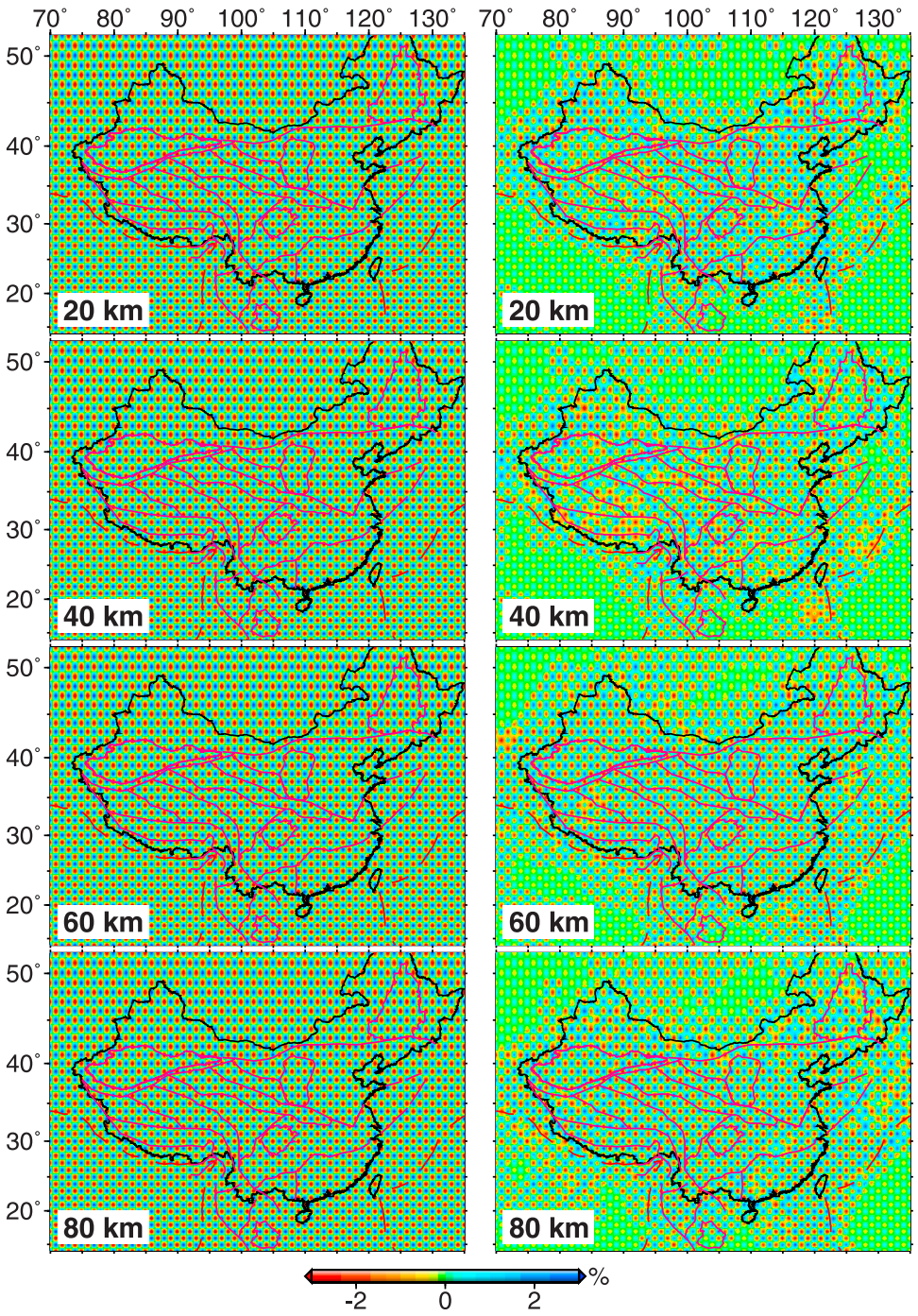

Figure 12. (left) Input checkerboard and (right) results when the grid shown in Figure 5 is adopted. The depth of the layer is shown at the lower left corner of each map. Blue and red squares denote high and low velocities, respectively. The velocity perturbation scale is shown at the bottom.

traveltimes from the GT events. To test the eastern China velocity model, we selected one well-located earthquake (M 6.4) in the northern part of China that is recorded by more than 100 stations. The event occurred on 3 May 1996 with the epicenter at (40.72°N, 109.57°E), depth of 28 km and origin time 0332:46.3 UT, given in the ABCE. Our relocation of this event using arrival times from the 3-D velocity model is (40.72°N, 109.58°E) at a depth of 25 km and origin time 0332:45.9 UT. The ABCE data for the event and our relocation are shown in Table 3.

[27] The hypocentral difference between our location and the ABCE location is about 3.5 km, larger than the averaged hypocentral misfit of 0.9 km for the northwestern China GT events, but within the GT5 confidence bounds for this event. The origin time difference is 0.04 sec. The traveltime residuals, between the observed and predicted *P* wave traveltimes within 20° source-station separation, are much smaller using our final 3-D model than AK135. The mean traveltime residual is 1.89 s for AK135 and it is only 0.09 s for our final model. The standard deviation of traveltime

Table 1. Eleven GT Events in Northwest China[a]

Event	Date	Time, UT	Latitude, deg	Longitude, deg	Error, km		
					3-D	1-D	AK135
1	6 May 1990	0759:59.25	41.5618	88.7183	0.3	6.2	18.9
2	16 Aug 1990	0459:59.26	41.5392	88.7445	0.9	9.5	23.0
3	21 May 1992	0459:59.06	41.5419	88.7678	0.6	8.7	18.4
4	25 Sep 1992	0800:00.02	41.7167	88.3767	0.8	9.1	17.8
5	5 Oct 1993	0159:57.92	41.5922	88.7035	1.0	9.3	19.1
6	10 Jun 1994	0625:59.46	41.5271	88.7074	0.9	8.1	18.4
7	7 Oct 1994	0325:59.44	41.5741	88.7256	0.7	7.7	19.6
8	15 May 1995	0405:59.38	41.5545	88.7516	0.6	8.8	24.9
9	17 Aug 1995	0059:59.35	41.5402	88.7533	0.7	9.2	18.8
10	8 Jun 1996	0255:59.37	41.5780	88.6875	0.9	9.3	20.1
11	29 Jul 1996	0148:59.62	41.7162	88.3757	0.4	8.4	21.5

[a]The relocation errors (hypocentral) are listed in km. Events are relocated using our new *P* wave model, the averaged 1-D model in China, and the surrounding area and the standard AK135 (global).

residuals is 1.2 s for AK135 and it is 0.49 s for our final model.

5. Discussion and Conclusions

[28] Strong *P* wave velocity variations of more than 10% found in the study area indicate the existence of significant structural heterogeneities in the crust and uppermost mantle in this region. At shallow depth (the 10 km slice in Figure 8), velocity images in the North China Block, the South China Block, the Sichuan Basin, the Ordos Basin, the Tarim Basin, and the Tianshan regions exhibit different patterns. In the North China Block, a low-V anomaly is found beneath the Songliao Basin and a high-V anomaly is imaged beneath the Bohai Gulf region. Low-V zones underlie most of the Tianshan region and Tarim Basin though a high-V zone exists in the center of the Sichuan Basin. In the South China Block we find a high-V anomaly in the south and low-V zones in the north. Beneath the mountains surrounding the Ordos Basin in the north, west and east, a high-V anomaly is found at the depth of 10 km. The center of the Ordos basin shows a low-V anomaly. As a whole, the velocity images of shallow layers correlate well with the surface geology, topography, and lithology.

[29] Our initial *Pn* velocities were constructed based on the *Pn* structure of the 1-D Monte Carlo search [*Sun et al.*, 2004b]. Here we compare the *Pn* velocities obtained by *Hearn et al.* [2004], the 1-D Monte Carlo search, and final 3-D structure (Figure 7). The prominent low *Pn* zones in eastern China are consistent throughout all the *Pn* models. Southern and eastern areas of Tibet show a high *Pn* velocity. We also observe a high *Pn* velocity beneath the Sichuan Basin, Ordos Basin and Tianshan area. The discrepancies are mostly in the Tibetan region. *Hearn et al.* [2004] observed a high *Pn* velocity beneath the Qilian and the Kunlun area, though we only observe a high *Pn* beneath the eastern Qilian in our final model. Some parts of the Kunlun area show high *Pn* velocity. This discrepancy might be caused by the overaveraging effect of the 1-D inversion. The high *Pn* in the eastern Tibet is carried over to the western part due to the sparse ray coverage in the western part and very large windows that are selected to provide averaged 1-D profiles in the Monte Carlo inversion.

[30] The Moho discontinuity plays an important role in tomography. The importance of taking into account the Moho depth variations and other discontinuities in the tomographic inversion has also been demonstrated in the earlier studies of the Japan and Tonga subduction zones [*Zhao et al.*, 1992, 1997], southern Carpathians, Romania [*Fan et al.*, 1998], and southwest China [*Huang et al.*, 2002]. When the discontinuity topography is taken into account, ray paths and traveltimes can be computed more accurately, and therefore a better tomographic result is expected. *Sun* [2005] shows that the final RMS traveltime residual is 0.58 s for the inversion when the Moho topography is considered, 6% lower than the 0.62 s RMS residual with the flat Moho (50 km), the average Moho depth in the study area (Figure 7).

[31] While the Moho depths are fixed as the initial model in our inversion, *Sun* [2005] conducts an inversion by allowing the Moho depths to change between −5 and 5 km of the initial model, and both Moho depths and velocities are unknowns in the inversion. The Moho depth difference is within ±1 km and the *Pn* velocity difference is within ±0.1 km/s compared to the reference 3-D model. Along a vertical cross section (profile E in Figure 10) the final velocity difference is within ±0.1 km/s in the crust and uppermost mantle. The Moho depth difference along the profile E is within ±1 km throughout the cross section.

[32] In summary, our velocity model shows the following features:

[33] 1. The seismic velocity images are characterized by block structures corresponding to geological features bounded by large fault zones. This region consists of a few geological structures: the North China Block including Songliao Basin, the South China Block, the Sichuan Basin,

Table 2. Comparison of the Traveltime Residuals Based on Different Models[a]

Traveltime Residuals	Final 3-D	Input 3-D	Averaged 1-D	AK135
Mean, s	[−0.6, 0.6]	[−0.8, 0.8]	[−1, 1]	[−3, 3]
SD, s	[0.05, 0.15]	[0.05, 0.2]	[0.05, 0.3]	[0.1, 0.9]

[a]For each model, the range of the mean and standard deviation (SD) of traveltime residuals at each station are listed. The range of the means and SDs are listed for 50 stations about 20° from the events.

Table 3. Comparison of the Hypocentral Parameters of a Well-Constrained Earthquake in Northeastern China[a]

	Origin Time, UT	Latitude, deg	Longitude, deg	Depth, km
ABCE	0332:46.3	40.72	109.57	28
MIT	0332:45.9	40.72	109.58	25

[a]ABCE parameters are obtained from a dense network of local and regional stations and are estimated to be GT-5. MIT parameters are obtained by relocating the event using the new 3-D *P* wave velocity model.

the Tarim Basin, and the Tianshan area. Those areas exhibit different patterns of velocity distribution in the tomographic images. The trend of velocity anomalies is consistent with the trend of regional tectonics.

[34] 2. A clear dividing line along the 105° parallel separates China into a low-V zone in the west and a high-V zone in the east at a depth of 40 km.

[35] 3. Our tomographic imaging has revealed significant velocity heterogeneities in the middle and lower crust, some of which are consistent with those detected by deep seismic soundings and other geophysical investigations.

[36] 4. *Pn* velocities are high under southern and eastern Tibet, and under the Sichuan and Ordos basins.

[37] 5. Velocity heterogeneities below Moho at Indochina subduction zone reflect the tectonic history and ongoing subduction.

[38] **Acknowledgments.** This work was supported by the Defense Threat Reduction Agency under contract DTRA01-00-C-0024 and by Air Force Research Laboratory under contract FA8718-04-C-0018. Thanks to Dapeng Zhao and Jianshe Lei in Ehime University, Matsuyama, Japan, for the support on this research. We also thank John Chen and Shunping Pei from Peking University, Beijing, China, for their suggestions and comments. Anca Rosca, Mark Willis, Stephane Rondenay, Burke Minsley, and Maureen Long from MIT; Walter Mooney from USGS; and Charlotte Rowe and Michael Fehler from the Los Alamos National Laboratory provided great help on improving the manuscript. We are greatly indebted to Haijiang Zhang from University of Wisconsin–Madison, two anonymous reviewers, and the Associate Editor for their insightful comments. All the figures in this work are made by using GMT [*Wessel and Smith*, 1995].

References

China Seismological Bureau (1986), *Findings of Exploring the Crust and Upper Mantle Structure of China* (in Chinese), 407 pp., Seismol. Press, Beijing.

Eberhart-Phillips, D. (1986), Three-dimensional velocity structure in northern California Coast Ranges from inversion of local earthquake arrival times, *Bull. Seismol. Soc. Am.*, *76*, 1025–1052.

Fan, G., T. Wallace, and D. Zhao (1998), Tomographic imaging of deep velocity structure beneath the eastern and southern Carpathians, Romania: Implications for continental collision, *J. Geophys. Res.*, *103*, 2705–2723.

Fisk, M. D. (2002), Accurate locations of nuclear explosions at the Lop Nor test site using alignment of seismograms and IKONOS satellite imagery, *Bull. Seismol. Soc. Am.*, *92*, 2911–2925.

Hearn, T. M., S. Wang, J. F. Ni, Z. Xu, Y. Yu, and X. Zhang (2004), Uppermost mantle velocities beneath China and surrounding regions, *J. Geophys. Res.*, *109*, B11301, doi:10.1029/2003JB002874.

Huang, J., and D. Zhao (2004), Crustal heterogeneity and seismotectonics of the Chinese capital region, *Tectonophysics*, *385*, 159–180.

Huang, J., D. Zhao, and S. Zheng (2002), Lithospheric structure and its relationship to seismic and volcanic activity in southwest China, *J. Geophys. Res.*, *107*(B10), 2255, doi:10.1029/2000JB000137.

Huang, Z., W. Su, Y. Peng, Y. Zheng, and H. Li (2003), Rayleigh wave tomography of China and adjacent regions, *J. Geophys. Res.*, *108*(B2), 2073, doi:10.1029/2001JB001696.

Institute of Geophysics, China Seismological Bureau (IG-CSB) (1990–2003), Annual bulletin of Chinese earthquakes (ABCE), Seismol. Publ. House, Beijing.

Kissling, E., W. L. Ellsworth, D. Eberhart-Phillips, and U. Kradolfer (1994), Initial reference models in local earthquake tomography, *J. Geophys Res.*, *99*, 19,635–19,646.

Laske, G., and G. Masters (1997), A global digital map of sediments thickness (abstract), *Eos Trans. AGU*, *78*(46), Fall Meet. Suppl., F483.

Lebedev, S., and G. Nolet (2003), Upper mantle beneath Southeast Asia from *S* velocity tomography, *J. Geophys. Res.*, *108*(B1), 2048, doi:10.1029/2000JB000073.

Leveque, J., L. Rivera, and G. Wittlinger (1993), On the use of the checkerboard test to assess the resolution of tomographic inversions, *Geophys. J. Int.*, *115*, 313–318.

Li, C., R. D. van der Hilst, and M. N. Toksöz (2006), Constraining *P*-wave velocity variations in the upper mantle beneath Southeast Asia, *Phys. Earth Planet. Inter.*, *154*, 180–195.

Li, S., X. Zhang, and Z. Song (2001), Three-dimensional crustal structure of the capital area obtained by a joint inversion of deep seismic sounding data from multiple profiles (in Chinese), *Acta Geophys. Sin.*, *44*, 360–368.

Liang, C., X. Song, and J. Huang (2004), Tomographic inversion of *Pn* traveltimes in China, *J. Geophys. Res.*, *109*, B11304, doi:10.1029/2003JB002789.

Liu, F. T., H. Wu, J. H. Liu, G. Hu, Q. Li, and K. X. Qu (1990), 3-D velocity images beneath the Chinese continent and adjacent regions, *Geophys. J. Int.*, *101*, 379–394.

Mooney, W. D. (1998), CRUST 5.1: A global crustal model at 5° × 5°, *J. Geophys. Res.*, *103*, 727–747.

Paige, C., and M. Saunders (1982), LSQR: An algorithm for sparse linear equations and sparse least squares, *Trans. Math. Software*, *8*, 43–71.

Pei, S., Z. Xu, and S. Wang (2004), Discussion on origin of *Pn* velocity variation in China and adjacent region (in Chinese), *Acta Seismol. Sin.*, *26*, 1–10.

Pei, S., Y. Chen, D. Zhao, A. Yin, J. Ning, and X. Chen (2006), Tomographic structure of east Asia and its geodynamic implication, *J. Geophys. Res.*, doi:10.1029/2004JB003332, in press.

Phillips, W. S., C. A. Rowe, and L. K. Steck (2005), The use of interstation *P* wave arrival time differences to account for regional path variability, *Geophys. Res. Lett.*, *32*, L11301, doi:10.1029/2005GL022558.

Ritzwoller, M. H., M. P. Barmin, A. Villasenor, A. L. Levshin, and E. R. Engdahl (2002), *Pn* and *Sn* tomography across Eurasia to improve regional seismic event locations, *Tectonophysics*, *358*, 39–55.

Shapiro, N. M., and M. H. Ritzwoller (2002), Monte Carlo inversion for a global shear velocity model of the crust and upper mantle, *Geophys. J. Int.*, *151*, 88–105.

Song, Z. H., C. Q. An, G. Y. Chen, L. H. Chen, Z. Zhuang, Z. W. Fu, and J. F. Hu (1991), Study on 3-D velocity structure and anisotropy beneath west China from the Love wave dispersion (in Chinese), *Acta Geophys. Sin.*, *34*, 694–707.

Stevens, J. L., D. A. Adams, and G. E. Baker (2001), Improved surface wave detection and measurement using phase-matched filtering with a global one-degree dispersion model, paper presented at 23rd Seismic Research Review: Worldwide Monitoring of Nuclear Explosions, Natl. Nucl. Secur. Admin., Jackson Hole, Wyo. (Available at https://www.nemre.nnsa.doe.gov/cgi-bin/prod/researchreview/index.cgi?Year=2001)

Sun, R., and F. Liu (1995), Crust structure and strong earthquakes in Beijing, Tianjin and Tanshan area. I. *P* wave velocity structure (in Chinese), *Acta Geophys. Sin.*, *38*, 599–607.

Sun, Y. (2005), *P*- and *S*-wave tomography of the crust and uppermost mantle in China and surrounding areas, Ph.D. thesis, Mass. Inst. of Technol., Cambridge.

Sun, Y., S. Kuleli, F. D. Morgan, W. Rodi, and M. N. Toksöz (2004a), Location robustness of earthquakes in Sichuan province, China, *Seismol. Res. Lett.*, *75*(1), 54–62.

Sun, Y., X. Li, S. Kuleli, F. D. Morgan, and M. N. Toksöz (2004b), Adaptive moving window method for 3-D *P*-velocity tomography and its application in China, *Bull. Seismol. Soc. Am.*, *94*, 740–746.

Um, J., and C. Thurber (1987), A fast algorithm for two-point seismic ray tracing, *Bull. Seismol. Soc. Am.*, *77*, 972–986.

Wang, C.-Y., W. W. Chan, and W. D. Mooney (2003), Three-dimensional velocity structure of crust and upper mantle in southwestern China and its tectonic implications, *J. Geophys. Res.*, *108*(B9), 2442, doi:10.1029/2002JB001973.

Wessel, P., and W. Smith (1995), New version of the generic mapping tools released, *Eos Tran. AGU*, *76*, 329.

Wu, F. T., A. L. Levshin, and V. M. Kozhevnikov (1997), Rayleigh wave group velocity tomography of Siberia, China, and vicinity, *Pure Appl. Geophys.*, *149*, 447–473.

Xu, Y., F. Liu, J. Liu, and H. Chen (2002), Crust and upper mantle structure beneath western China from *P* wave travel time tomography, *J. Geophys. Res.*, *107*(B10), 2220, doi:10.1029/2001JB000402.

Yu, X., Y. Chen, and P. Wang (2003), Three-dimensional *P* wave velocity structure in Beijing -Tianjin-Tangshan area, *Acta Seismol. Sin.*, *25*, 1–14.

Zhao, D. (2001), New advances of seismic tomography and its applications to subduction zones and earthquake fault zones: A review, *Island Arc*, *10*, 68–84.

Zhao, D., A. Hasegawa, and S. Horiuchi (1992), Tomographic imaging of P and S wave velocity structure beneath northeastern Japan, *J. Geophys. Res.*, *97*, 19,909–19,928.

Zhao, D., A. Hasegawa, and H. Kanamori (1994), Deep structure of Japan subduction zone as derived from local, regional, and teleseismic events, *J. Geophys. Res.*, *99*, 22,313–22,330.

Zhao, D., Y. Xu, D. Wiens, L. Dorman, J. Hilderbrand, and S. Webb (1997), Depth extent of the Lau back-arc spreading center and its relation to subduction processes, *Science*, *278*, 254–257.

Zhu, J., J. Cao, X. Cai, Z. Yan, and X. Cao (2002), High resolution surface wave tomography in east Asia and west Pacific marginal sea, *Chin. J. Geophys.*, *45*, 679–698.

Zhu, L., R. Zeng, and F. Liu (1990), 3-D *P* wave velocity structure under the Beijing network area (in Chinese), *Acta Geophys. Sin.*, *33*, 267–277.

Y. Sun and M. N. Toksöz, Earth Resources Laboratory, Department of Earth, Atmospheric, and Planetary Sciences, Massachusetts Institute of Technology, E34-566, 42 Carleton Street, Cambridge, MA 02142-1324, USA. (youshun@mit.edu)